

pp 24–43. © Royal Aeronautical Society 2019  
doi:10.1017/aer.2019.135

# Estimation of three-dimensional aerodynamic damping using CFD

R.J. Higgins<sup>1</sup> and G.N. Barakos<sup>2</sup>  
[george.barakos@glasgow.ac.uk](mailto:george.barakos@glasgow.ac.uk)

University of Glasgow  
Glasgow  
U.K.

## E. Jinks

Dowty Propellers, Anson Business Park  
Gloucester  
U.K.

## ABSTRACT

Aeroelastic phenomena of stall flutter are the result of the negative aerodynamic damping associated with separated flow. From this basis, an investigation has been conducted to estimate the aerodynamic damping from a time-marching aeroelastic computation. An initial investigation is conducted on the NACA 0012 aerofoil section, before transition to 3D propellers and full aeroelastic calculations. Estimates of aerodynamic damping are presented, with a comparison made between *URANS* and *SAS*. Use of a suitable turbulence closure to allow for shedding of flow structures during stall is seen as critical in predicting negative damping estimations. From this investigation, it has been found that the *SAS* method is able to capture this for both the aerofoil and 3D test cases.

**Keywords:** Flutter; damping; moment loop; aeroelasticity

## NOMENCLATURE

$c_{ref}$	reference blade chord (m)
$C_m$	pitching moment coefficient (-)
$f_s$	sampling frequency (Hz)
$k$	reduced frequency (-)
$\vec{n}$	normal vector (-)
$\tilde{p}$	unsteady surface pressure coefficient (-)
$R$	blade radius (m)

$R/c$	blade aspect ratio (-)
$\vec{u}$	non-dimensional local displacement velocity (-)
$W$	aerodynamic work (-)

### Greek Symbol

$\alpha$	Angle-of-attack (°)
$\alpha_h$	Harmonic Pitching Angle (°)
$\alpha_o$	Mean Pitch Angle (°)
$\theta_{cycle}$	Aerodynamic Damping (-)
$\tau$	Non-dimensional Time (-)
$ \hat{\omega} $	Non-dimensional Vorticity Magnitude (-)

### Acronyms

<i>CFD</i>	Computational Fluid Dynamics
<i>CSD</i>	Computational Structural Dynamics
<i>HMB3</i>	Helicopter Multi-Block Solver 3
<i>SAS</i>	Scale-Adaptive Simulation
<i>URANS</i>	Unsteady Reynolds-Averaged Navier-Stokes

### Superscripts

$D, U$	Downstroke/Upstroke
--------	---------------------

## 1.0 INTRODUCTION TO AERODYNAMIC DAMPING ESTIMATION

Aerodynamic damping is the result of forces and moments exerted on to a structure due to aerodynamics. Aerodynamic damping often opposes structural damping, and can potentially result in aeroelastic instabilities. Aerodynamic damping is often critical to the flutter characteristics of a structure. Above the flutter velocity, the work of the given fluid on a structure is said to be negatively damped. Thus, the structure's oscillatory motions tend to increase with time.

Stall flutter originates from separated flow and is found to be present in helicopter rotors, propellers and other rotating wings. A stall flutter instability can only be corrected via positive structural damping or a change in the aerodynamic conditions. As a result, an investigation into stall flutter can begin from the aerodynamic damping of a system. Damping estimation is often performed for aerofoils and full three-dimensional calculations are rare.

Early investigations of stall flutter were two-dimensional, and experimental<sup>(1,2,3)</sup>. These investigations focused on determining the aerodynamic coefficients during dynamic stall phenomena for the purpose of improving helicopter performance in forward flight. Such 2D investigations of oscillating aerofoils highlighted the trends seen during differing stall regimes. These regimes are highlighted in Fig. 1 where the pitching moment coefficient trends are presented for a pitching NACA 0012 aerofoil.

**No Stall:** Within the no stall regime, the aerofoil motion remains below the static stall angle and the use of quasi-steady aerodynamic is sufficient enough to predict the aerofoil loading.

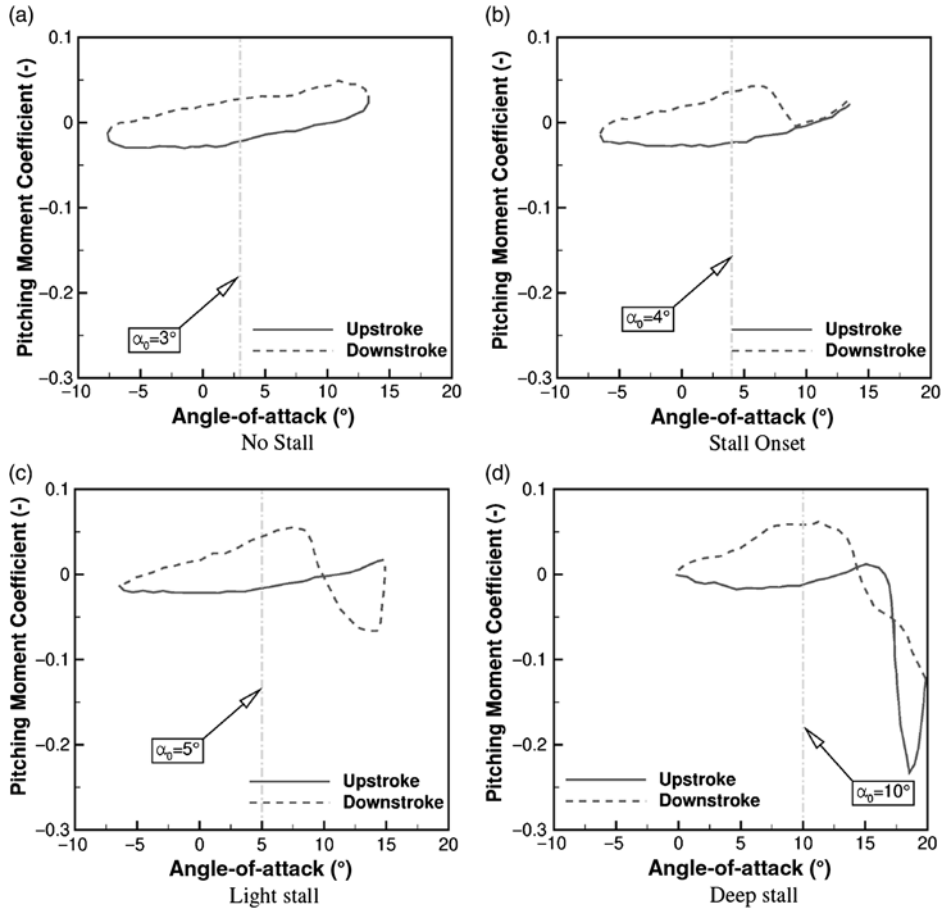


Figure 1. Pitching moment coefficient trends for each stall regime, as observed by McCroskey for a NACA 0012 aerofoil pitching at  $\alpha = \alpha_o + 10^\circ \sin(2k\tau)$ , where  $k = 0.10$ <sup>(3)</sup>.

Both the lift and pitching moment coefficients are found to circle in an anti-clockwise manner with no crossing of the downstroke and upstroke profiles.

**Stall Onset:** During this regime, the aerofoil motion reaches the static stall angle. There is often found a slight reduction within the area of the anti-clockwise loop, however, no crossing of the profiles are seen and therefore quasi-steady aerodynamic can be used to estimate the loads.

**Light Stall:** It is within this regime that dynamic stall vortices are present. For this regime, the aerofoil motion reaches values higher than the static stall angle, with the aerofoil loads characterised by a hysteresis effect. The development of separated flow regions are found to be sensitive to the aerofoil geometry, freestream Reynolds number and Mach number, reduced frequency of the aerofoil oscillation, and the mean and harmonic angles of attack. It is also within the regime that there is the highest tendency towards negative aerodynamic damping.

**Deep Stall:** For this regime, the aerofoil motion is often found to pitch entirely beyond the static stall angle and it is where the strongest effects of the dynamic stall vortex are seen. The aerofoil loading is characterised by a strong hysteresis effect, with significantly larger peak lift and moment coefficients.

During the light and deep dynamic stall regimes, three-dimensional effects become important as separated flows are often three-dimensional. As a result, two-dimensional experiments or fluid dynamic modelling lose their accuracy. From this basis, for highly stalled cases such as stalled aerofoil or helicopter rotor, high fidelity 3D aerodynamic modelling is required.

In addition to helicopter rotors, stall flutter may be present in propeller blades, particularly during aircraft take-off when the blade pitch is high. To date, very few experimental investigations have been conducted for propeller stall flutter. These include the Spitfire propeller<sup>(4)</sup>, the Commander propeller<sup>(5)</sup>, the SR blades<sup>(6)</sup>, along with some idealised models<sup>(7,8)</sup>. These investigations focused on static experiments, often with torsional stress levels measured to provide estimates of the flutter boundary. In addition to the experimental investigations, several numerical simulations have been conducted<sup>(9,10,11)</sup>, however, these investigations use two-dimensional aerodynamics. Stall in its essence is three-dimensional, and therefore, the use of two-dimensional aerodynamics can only provide an estimate of the mean aerodynamic loading. The fluctuations in pressure are key to the stall flutter prediction and these are not captured via two-dimensional aerodynamics. Subsequently, conservative boundaries are found by all numerical studies at high pitch angle<sup>(9,10,11)</sup>.

To improve understanding of three-dimensional effects on aerodynamic damping, and to understand which CFD methods are required for the investigation of stall flutter, the following investigation is conducted:

At first, a quasi-3D method is applied to a rigidly pitching aerofoil. The quasi-3D technique is based upon the assumption of an infinite wing, with a comparison made to standard two-dimensional modelling. In addition to the three-dimensional effects which are captured using periodic boundary conditions, the use of the quasi-3D technique also allows for the use of higher fidelity turbulence modelling in the form of Scale-Adaptive Simulation (SAS). The NACA 0012 dynamic stall database of McAlister<sup>(1)</sup> was selected due to the range of validation data available from this investigation, and its trust within the aerospace community.

Then, following the investigation on the NACA 0012, several of the Commander propeller blade aerofoil sections<sup>(5)</sup> are investigated for their levels of aerodynamic damping. Again, a comparison was made between standard *URANS* two-dimensional modelling to *SAS* quasi-3D methods.

Finally, a comparison of the quasi-3D Commander aerofoil section results is made to the fully three-dimensional aeroelastic stall flutter computation of the Commander propeller blade. The Commander propeller blade was selected for this investigation due to the availability of the geometry, test data and its trust by manufacturers due to its in-service application.

## 2.0 COMPUTATIONAL METHODOLOGY: HMB3

For this investigation, the in-house CFD solver HMB3 is used. The core functionality of HMB3 is CFD, however its use has been extended in recent years to include whole engineering applications, including helicopter rotor aeroelasticity<sup>(12)</sup> and propeller validation<sup>(13,14)</sup>. In addition to this, the time-marching aeroelastic method of HMB3 has been validated with respect to propeller stall flutter for the Commander propeller blade<sup>(15,16)</sup>.

### 2.1 Computational fluid dynamics

Previous investigations using HMB3 have provided propeller flow validation in both installed and isolated conditions, by comparison with the experimental results of the JORP

propeller<sup>(17)</sup> and the IMPACTA wind-tunnel tests<sup>(18,19)</sup>. Good agreement was found in terms of aerodynamics and acoustics<sup>(14,13)</sup>. HMB3 solves the Navier-Stokes equations in integral form and are discretised using a cell-centered finite volume approach on a multi-block grid. The spatial discretisation of these equations leads to a set of ordinary differential equations in time,

$$\frac{d}{dt}(\mathbf{W}_{i,j,k} V_{i,j,k}) = -\mathbf{R}_{i,j,k}(\mathbf{w}), \quad \dots (1)$$

where  $i, j, k$  represent the cell index,  $\mathbf{W}$  and  $\mathbf{R}$  are the vector of conservative variables and flux residual respectively and  $V_{i,j,k}$  is the volume of the cell  $i,j,k$ . Greater detail on the numerical techniques employed can be found within the previous investigations conducted using HMB3<sup>(12,13,14,20,21,22,23,24)</sup>. Several turbulence models, of both URANS and hybrid LES/URANS families, are available in the HMB3 solver. For this investigation the standard  $k - \omega$  turbulence model will be compared to the hybrid LES/URANS method known as Scale Adaptive Simulation (SAS)<sup>(26,27)</sup>. The SAS formulation allows for the dynamic adjustment of the von Karman length scale to produce an *LES-like* solution. HMB3 SAS simulations have been conducted in the past focusing on transonic cavity flows<sup>(25)</sup> and missile projection<sup>(28)</sup>. Because this investigation requires the deformation and relative motion of the propeller blade, in order to achieve this, the chimera method is used<sup>(29)</sup>. ICEM-Hexa<sup>TM</sup> of ANSYS is used to generate all structured grids for this investigation.

## 2.2 Computational structural dynamics

The aeroelastic framework of HMB3 is based on the modal method<sup>(16,24)</sup>. This method uses externally computed structural modes and a mesh deformation module based on the inverse distance weighting interpolation. The modal approach was selected in order to reduce computational cost as it expresses solid deformations as functions of the structure's eigenmodes.

A NASTRAN finite element model is created in order to obtain the structural mode shapes and frequencies. The finite element model uses non-linear PBEAM elements to model the structure's mass and inertia distribution along the span, with rigid bars (RBAR) elements used to connect the PBEAM node to each of the fluid mesh points at the given section. A non-linear static analysis (SOL 106) is computed to obtain the mode shapes and frequencies, along with a static deformation to rigid loads.

At the beginning of each computation, the structural modes are interpolated from the CSD to the CFD grid. The interpolation is performed with the Moving Least Square method (MLS). The MLS method allows for sufficient accuracy in terms of the modal force and displacement estimations due to the fact these values are calculated based upon the CFD grid without further interpolation to the CSD.

## 3.0 TWO-DIMENSIONAL AERODYNAMIC DAMPING

Very few 2D cases have been computed for specific propeller sections to allow for the introduction of the SAS approach for the calculation of aerodynamic damping. As a result, the NACA 0012 section was selected due to the amount of experiment data available at different pitching conditions. The 70%R and 90%R Commander aerofoils were also investigated to provide a comparison with the NACA 0012 for a specific propeller section.

## 3.1 2D aerodynamic damping calculation

To fully determine the stability of the aerofoil section, the amount of aerodynamic damping within the system can be computed via the integration of the pitching moment coefficient with respect to the pitching angle. Such a method was described by Corke in 2015<sup>(30)</sup> with the derivation of the aerodynamic damping shown in Equation 2, where  $C_m^D$  and  $C_m^U$  are the pitching moment coefficients on the downstroke and upstroke, respectively, and  $\alpha_h$  is the harmonic pitching angle.

$$\theta_{cycle} = \frac{1}{\pi \alpha_h^2} \int (C_m^D - C_m^U) d\alpha \quad \dots (2)$$

## 3.2 Computational setup

### 3.2.1 NACA 0012 section

The topology of the grid follows a traditional C-grid type with a downstream far-field boundary applied at 15 chords from the trailing edge. In terms of the mesh, 650 cells were distributed around the aerofoil with 85 cells distributed via an exponential law, clustering to  $1 \times 10^{-6} C_{ref}$ , outward of the aerofoil surface.

Standard two-dimensional boundary conditions were applied to the spanwise boundary faces for an initial verification of the mesh quality and CFD setup, with a single computational cell in the spanwise direction of length 1 chord. A single chord spanwise length was selected due to the ease of non-dimensional load scaling within HMB3. Following this, the two-dimensional conditions were replaced with periodic boundary conditions. This allows for quasi-3D simulations where scale-resolving turbulence modelling can be implemented. For this investigation standard *URANS* closed with the  $k - \omega$  shear-stress-transport (SST) turbulence model was compared to *SST-SAS*. No difference in aerofoil loads was observed between the 2D and quasi-3D simulations using the standard *URANS* formulation, hence, only the 2D *URANS* loads are presented. For the quasi-3D simulations, the spanwise length was set to a quarter of the chord. A quarter chord is selected based upon the findings of the LESFOIL project<sup>(31)</sup>. For accurate turbulence production from scale-resolving methods, the spanwise extend of the aerofoil must not be greater than a quarter of the chord.

The test conditions for this calculation are presented in Table 1 and correspond to experiments by McAlister in 1982<sup>(1)</sup>. These test conditions were selected as they represent typical flow conditions found during the dynamic stall of a helicopter rotor in forward flight and based upon the experimental report, these test conditions were found to have negative aerodynamic damping.

### 3.2.2 Commander aerofoil section

In a similar manner to the NACA 0012 investigation, a matched grid was derived for the Commander 70%*R* and 90%*R* sections with similar topology, number of grid points and points distribution used. Subtle modifications to the NACA 0012 mesh are required to account for the blunt trailing edge on the Commander sections.

For the Commander sections, the same computational setup, in terms of time-step, pseudo steps, CFL and turbulence modelling, as the NACA 0012 case is selected. Standard 2D and quasi-3D simulations were conducted. The selected test conditions for the Commander sections are presented in Table 1. These test conditions were selected based upon the Mach

**Table 1**  
**Test conditions for the dynamic stall computations**

Parameter	<i>NACA 0012</i>	<i>70%R</i>	<i>90%R</i>
Reynolds number	$2.42 \times 10^6$	$1.8 \times 10^6$	$2.0 \times 10^6$
Mach number	0.184	0.44	0.57
Reduced frequency	0.149	0.18	0.12
Pitching motion	$15^\circ \pm 10^\circ \sin(2k\tau)$	$12^\circ \pm 5^\circ \sin(2k\tau)$	$8^\circ \pm 5^\circ \sin(2k\tau)$
Steps per revolution		1600	
Pseudo-steps		200	
Modelling		<i>URANS k – <math>\omega</math> SST &amp; SAS</i>	

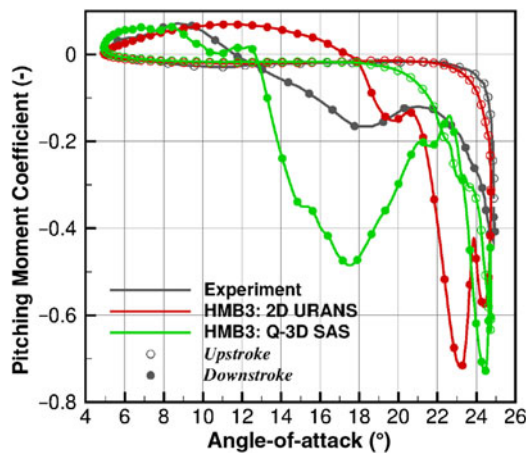


Figure 2. Comparison of the NACA 0012 pitching moment coefficient for the 2D and quasi-3D simulations to the experiment, with the flow conditions presented in Table 1.

number and pitch angle seen by the 3D blade, with a harmonic pitch angle of  $5^\circ$  selected to determine its response. All *SAS* simulation results were phased averaged over 4 revolutions before comparing to standard *URANS*.

### 3.3 NACA 0012 quasi-3D results

Presented in Fig. 2 is the pitching moment coefficient results for the NACA 0012 test case, comparing 2D *URANS* and phase-averaged quasi-3D *SAS*, to experiments.

In the experimental results, the pitching moment remains almost constant up until  $22^\circ$ , where it starts to increase, with the peak pitching moment coefficient observed at the maximum angle of  $25^\circ$ . A similar response is found with the 2D *URANS* simulation, however, the peak pitching moment is found to be greater. Based upon the 2D *URANS* results, this response is seen to be based upon the development of stalled flow across the aerofoil trailing edge. This is observed in the flow visualisation results of Fig. 3(a,c,e). The negative pitching moment for the quasi-3D *SAS* simulation is found to increase earlier at  $18^\circ$ , and this correlates with an increase in the developed detached flow. Fig. 3(b,d,f) highlight the earlier development of



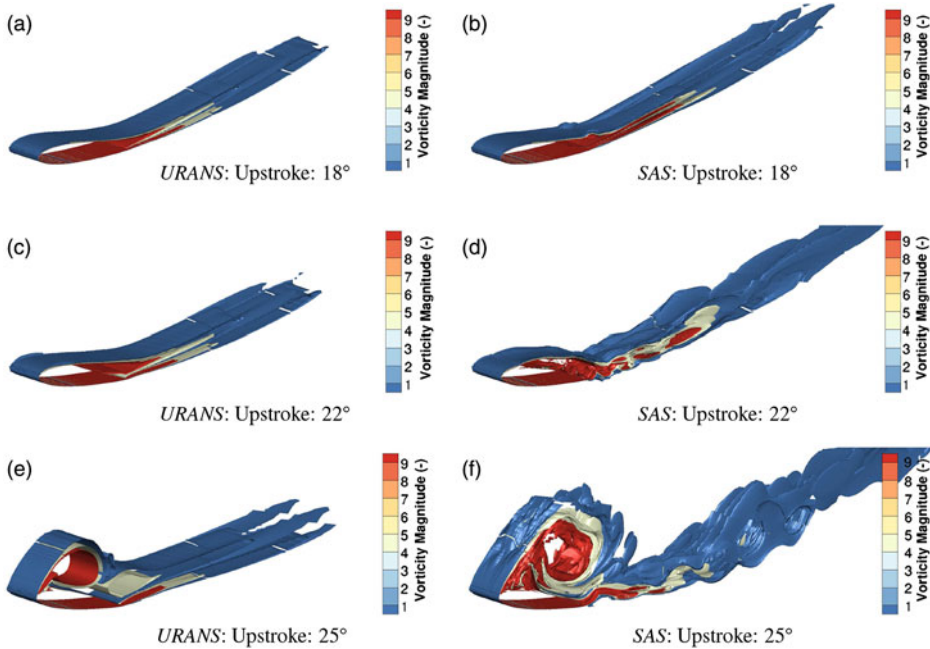


Figure 3. Flow visualisation of  $|\hat{\omega}| = [1.0, 5.0, 10.0]$  iso-surfaces during the aerofoil upstroke.

detached flow, particularly at  $22^\circ$  where the stalled flow is seen to be further upstream towards the leading-edge for the quasi-3D *SAS* result in comparison to the 2D *URANS*.

The recovery of the pitching moment during the experiment is found to occur over a range of  $13^\circ$ , eventually recovering and crossing the upstroke profile around  $12^\circ$ . During the downstroke, the 2D *URANS* is found to have a significant secondary stall event, resulting in two pitching moment peaks. The 2D *URANS* then quickly recovers, crossing the upstroke profile  $6^\circ$  earlier than experiments at  $18^\circ$ . This indicates that the 2D *URANS* simulation develops a closed stall bubble. This sheds from the section quickly, allowing the flow to attach at an earlier pitch angle than seen during the experiment. This is observed in the flow-field visualisation results for the *URANS* simulation in Fig. 4(a,c,e). For the quasi-3D *SAS*, following the peak, the pitching moment recovers to similar values as the experiment. The experimental pitching moment, during the downstroke, is seen to increase around  $18^\circ$ . This indicates the development of further separated flow between the  $22^\circ - 18^\circ$  range, as observed in Fig. 4(b,d,f). This is also present in the quasi-3D *SAS* simulation, however, the magnitude of this secondary event is found to be larger. The quasi-3D *SAS* simulation then begins to recover crossing the upstroke profile at the same angle as experiments. An average variation of  $\pm 0.5^\circ$  is found for the recovery angle, thus resulting in the closer estimation to the experimental recovery angle for the phased-averaged quasi-3D *SAS* than the 2D *URANS* simulations.

This variation in recovery angle is the result of cycle-to-cycle differences in the pitching moment coefficient for the quasi-3D *SAS* simulation. Cycle-to-cycle variations in dynamic stall experimental data has been discussed recently by Ramasamy et al.<sup>(32)</sup> They analysed two sets of experimental data and found that traditional phase-average filtering is not effective enough to represent dynamic stall load measurements. As a result, two new data-driven algorithms were developed to cluster the load results based upon the developed flow



**Table 2**  
**NACA 0012 aerodynamic damping**

Section	Modelling method	Aerodynamic damping
NACA 0012	Experiment	-0.350
	2D <i>URANS</i>	-0.204
	Quasi-3D <i>SAS</i>	-0.457

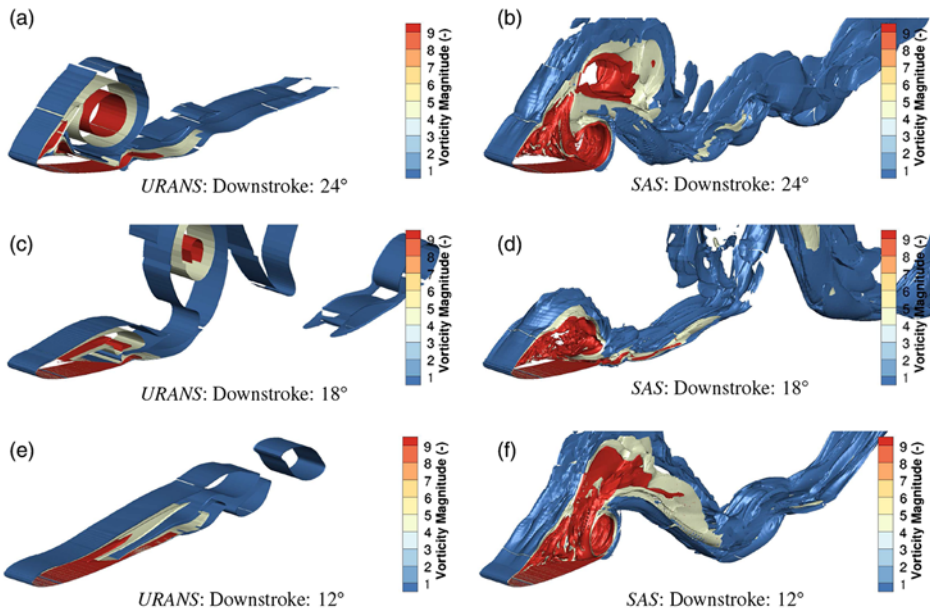


Figure 4. Flow visualisation of  $|\hat{\omega}| = [1.0, 5.0, 10.0]$  iso-surfaces during the aerofoil downstroke.

phenomena. Significant differences were found in the aerodynamic damping and load results between the two new clusters and the traditional phased-averaged solutions. From this study it is clear that an improvement in the analysis of experimental results is required to ensure the correct flow physics is captured.

Using the pitching moment curve, the aerodynamic damping of the system is estimated and presented in Table 2. As expected from the experimental report, a negative damping value is seen for both 2D *URANS* and quasi-3D *SAS* simulations. However, due to the sharp recovery of the 2D *URANS* simulation, the positive anti-clockwise moment loop is greater than seen from the experiment, therefore the damping estimation is below the experiment. The quasi-3D *SAS* simulation provides a larger negative damping value for the phased average solution, at a closer percentage to the experiment than the 2D *URANS*. In addition, a scatter in the estimated aerodynamic damping of  $\pm 37\%$  is observed per revolution, thus resulting in a closer estimation to the experimental results.

One of the objectives of this investigation was to determine which method, 2D *URANS* or quasi-3D *SAS*, best captures the characteristics associated with stall flutter. Based upon the aerodynamic loads, the 2D *URANS* performs better during the upstroke with the pitching moment coefficient increasing at the same position as the experiment. However, it is the

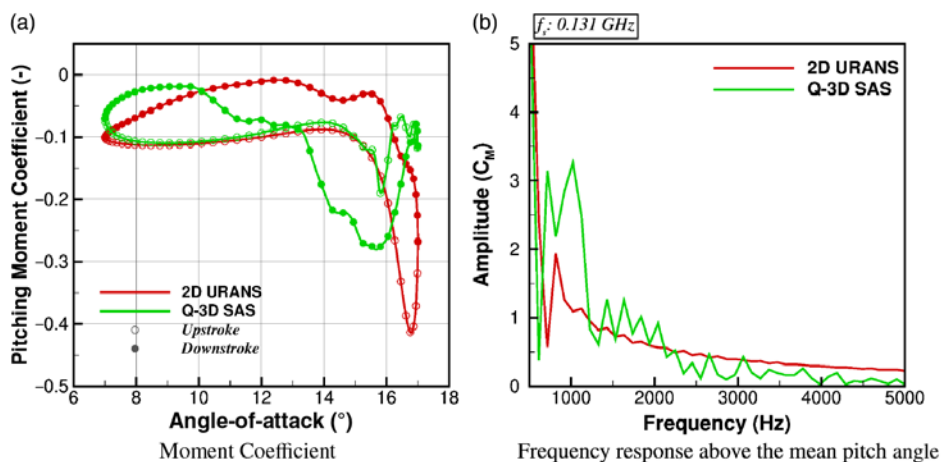


Figure 5. Pitching moment response of the 70%R Commander aerofoil section.

downstroke segment of the oscillation that has the greatest effect on the level of aerodynamic damping due to the amount of unsteady flow features present during this stage. On this basis, the quasi-3D *SAS* simulation performs better as the levels of aerodynamic damping better represent what was seen in the experiment. Overall, neither *URANS* or *SAS* are perfect for dynamic stall predictions, though the *SAS* appears to be better in representing the separated flow and this is important in the present investigation.

## 3.4 Commander aerofoil 2D aerodynamic damping estimation

### 3.4.1 70% radial station

Presented in Fig. 5(a) is the pitching moment coefficient of the Commander propeller section of the 70% radial station. As can be seen from the 2D *URANS* simulation results, a stable pitching moment profile is derived. During the upstroke, an almost constant negative pitching moment of  $-0.1$  is seen up until  $15^\circ$ . Following this, the aerofoil section separates causing the increase in negative pitching moment. Following the shedding of the developed closed stall bubble, the pitching moment recovers within  $1^\circ$ . As a result of this sharp recovery, the pitching moment loops do not cross, and hence, a stable anti-clockwise loop is derived.

For the quasi-3D *SAS* simulation, similar values of pitching moment are found during the upstroke, with the same stall angle of  $15^\circ$ . Following the initial stall, the detached flow is shed resulting in a small recovery/reattachment of the flow-field. As the angle-of-attack is increased further, detached flow again develops and vortices are shed from the aerofoil, accumulating during the peak pitching moment. The quasi-3D *SAS* simulation recovers around  $12^\circ$ . Due to this initial recovery on the upstroke, a negative clockwise moment loop is derived, resulting in negative aerodynamic damping, as shown in Table 3. The 2D *URANS* shows a stable solution.

A Fast-Fourier-Transform was conducted on the pitching moment coefficient results above the mean angle-of-attack of  $12^\circ$ , with the results presented in Fig. 5(b). For these simulations, a sampling frequency of  $0.131 \text{ GHz}$  is used, thus resulting in a maximum available frequency of  $0.066 \text{ GHz}$ . The Nyquist theorem is therefore satisfied for these comparisons. For the 2D

**Table 3**  
70%*R* aerodynamic damping

Section	Modelling method	Aerodynamic damping
RC070	2D: <i>URANS</i>	0.614
	Quasi-3D: <i>SAS</i>	-0.045

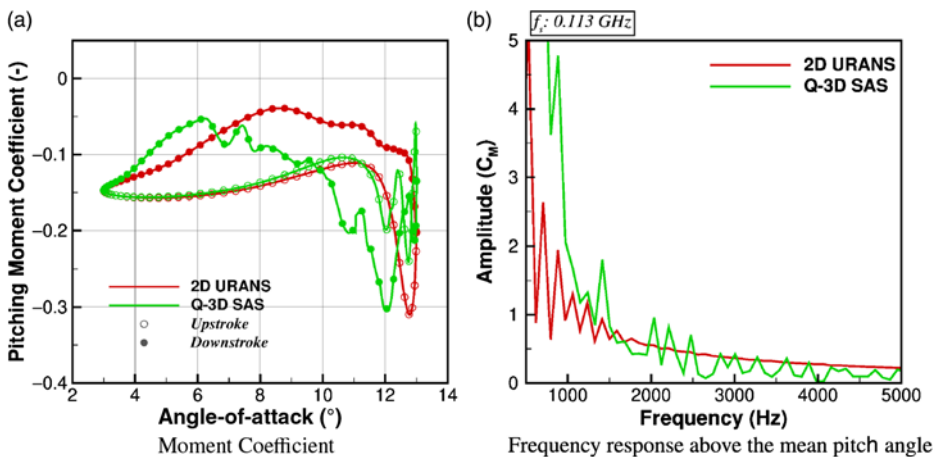


Figure 6. Pitching moment response of the 90%*R* Commander aerofoil section.

*URANS* result, a single peak at 1kHz is found and this corresponds to the peak moment coefficient. A similar peak is found in the quasi-3D *SAS* simulation, however, due to the double stall event, a double peak is observed from the frequency response with the frequency band ranging from 0.7 to 1.4kHz. At higher frequencies, several oscillations from the quasi-3D *SAS* simulation are observed. This is expected to due to the resolution of scales not captured via *URANS* and the oscillations in pitching moment coefficient seen at the maximum pitch angle. Some small oscillations are present at higher frequencies for the 2D *URANS* case, however, these are negligible in comparison to the quasi-3D *SAS* response.

### 3.4.2 90% radial station

Similar responses are found between the 2D *URANS* and quasi-3D *SAS* simulations. A full anti-clockwise moment loop is found, and presented, in Fig. 6(a) for the 2D *URANS* simulation. The pitching moment begins to increase around 11°. This is 3° above the mean angle-of-attack. The pitching moment recovers almost instantly resulting in a stable moment loop.

In a similar manner to the 70% station, after the pitching moment begins to increase, and the detached flow develops, the flow-field is shed from the station resulting in a recovery of the pitching moment for the quasi-3D *SAS* simulation. Several vortices from the detached flow are shed and this gives oscillating pitching moment as the section reaches the maximum angle-of-attack. During the downstroke, the pitching moment increases producing an unstable clockwise moment loop. The pitching moment recovers around the mean angle-of-attack.

**Table 4**  
**Aerodynamic damping**

Section	Modelling method	Aerodynamic damping
RC090	2D: <i>URANS</i>	0.497
	<i>Quasi-3D SAS</i>	0.104

The resultant anti-clockwise moment loop causes a reduction in the aerodynamic damping, presented in Table 4.

The frequency response for the pitching moment curve above the mean angle-of-attack of  $8^\circ$  is presented in Fig. 6(b). The sampling frequency was reduced to 0.113GHz due to the increase in sample time-step. This sampling frequency still satisfies the Nyquist theorem in order for a comparison to be made. For the 2D *URANS* simulation, several peaks are observed below 1kHz, with the highest amplitude seen at 0.6kHz. The quasi-3D *SAS* simulation produces a two high amplitude peaks at 0.75 and 1.2kHz, corresponding to the two stall events.

### 3.5 Summary of the two-dimensional aerodynamic damping investigation

It is concluded that the use of the *SAS* method provides a more realistic representation of the negative aerodynamic damping associated with stall flutter, as seen from the NACA 0012 damping estimations. Therefore, to conduct a stall flutter investigation, it is vital that scale-resolving aerodynamics are used which captures the fluctuations in surface pressure associated with vortex shedding.

## 4.0 THREE-DIMENSIONAL AERODYNAMIC DAMPING

Using the derived time-marching aeroelastic method, the Commander blade is modelled in isolation. This test case was selected due to the high torsional response seen in tests<sup>(5)</sup>. During model implementation, simulations were conducted utilising the full propeller, nacelle, wing combination, however, due to the large computational cost associated with such a simulation, and due to the fact that it is the detached flow associated with the reference blade that triggers the aeroelastic excitation (the excitation is then propagated to the additional blades via the nacelle connection with a phase difference seen within the excitation between blades), periodicity in space is assumed. This allows for the reduction of the computational domain to one propeller blade.

The baseline propeller design consisted of three blades, with an aspect ratio of  $\sim 11.0$ , and reference tip chord of  $\sim 0.13\text{m}$ .

### 4.1 3D aerodynamic damping calculation

To determine the stability of the propeller blade, the amount of aerodynamic work ( $W$ ) can be used. This involves the integration of the unsteady surface pressure ( $\bar{p}$ ) and local displacement velocity ( $\bar{u}$ ) over time (Equation 3). A test case which has a negative aerodynamic damping

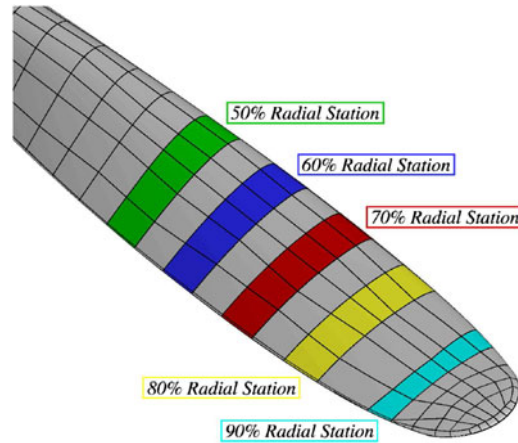


Figure 7. Commander propeller sections used for the damping calculations.

value, i.e. a destabilising flow, will have positive aerodynamic work. This method is used to determine the stability of the entire blade.

$$W = \int (\tilde{p} \cdot (\tilde{u} \cdot \tilde{n})) d\tau \quad \dots (3)$$

To relate the three-dimensional calculation to the two-dimensional aerofoils, as per the two-dimensional aerofoil calculations, the moment curve of a propeller blade section is used to determine the stability of the section. For the two-dimensional calculations, a sinusoidal rigid motion is applied to the aerofoil and this determines the change in angle-of-attack. For a full three-dimensional aeroelastic simulation, a test case which is active in torsion is required to obtain this change in angle-of-attack for the estimation of the aerodynamic damping coefficient.

Due to the employed multi-block mesh, selected block faces along the propeller blade surface can be used to determine the current pitch angle and pitching moment. The instantaneous pitch angle is calculated based upon reference leading-edge and trailing-edge node positions from the rigid blade. Presented in Fig. 7 are the selected block faces for the Commander propeller blade from the 50% to 90% radial station. For this investigation, and as per the dynamic stall study, focus will remain on the 70% and 90% radial stations.

Based upon the derived pitching moment and pitch angle, the aerodynamic damping is estimated via Equation 4:

$$\theta_{cycle} = \int (C_m^{D*} - C_m^{U*}) \partial\alpha, \quad \dots (4)$$

where  $C_m^{D*}$  and  $C_m^{U*}$  are the pitching moment coefficients along the radial station minus the mean value observed for that section, with superscripts  $D$  and  $U$  indicating downstroke and upstroke, respectively. To determine the aerodynamic damping based upon a change in pitching moment, and therefore relate such aerodynamic damping estimations to the two-dimensional study, the mean value of the pitching moment is subtracted from the instantaneous to ensure the blade rotational effects become less influential.

**Table 5**  
**Grids used for mesh convergence study of the 3D aeroelastic cases**

Grid level	Coarse	Baseline	Fine
Total Grid Size ( <i>volume cells</i> )	1,597,508	12,780,064	18,857,888
Foreground	441,508	3,532,064	9,609,888
Background	1,156,000	9,248,000	9,248,000

**Table 6**  
**Summary of the Commander propeller blade test conditions**

Reynolds number (-)	$1.65 \times 10^6$
Starting propeller rotational velocity ( <i>rpm</i> )	1400
Final propeller rotational velocity ( <i>rpm</i> )	1750
Blade pitch angle ( $^\circ$ ) <sub>0.70R</sub>	27°40'
Altitude ( <i>m</i> )	Sea-level
Inflow velocity ( <i>m/s</i> )	0.0 ( <i>Static conditions</i> )
Tip velocity ( <i>m/s</i> )	197.36
Tip chord length ( <i>m</i> )	0.122
Turbulence model	URANS $k - \omega$ & SAS

## 4.2 Computational setup

Based upon the supplied geometry a computation domain of  $120^\circ$  was created with a radial distance from the origin of  $5 R/c$ . The inflow was selected to be also  $5 R/c$  with the outflow  $8 R/c$  from the origin in the vertical direction, this is shown in Fig. 8(b). A solid cylindrical hub was created to simplify the background topology with the hub extending the length of the computational domain, from inflow to outflow.

A chimera grid (Fig. 8a) was used to allow for the deflection of the blade during the aeroelastic computations. A C-O-grid was used for the foreground mesh, and this was due to the blunt trailing edge and blade tip design. The blade root section was cut at  $0.124 \frac{r}{R}$ . This station was selected to remove the need to mesh around the complex hub mounting structures and also ensure a sufficient amount of cells are placed radially inwards for the chimera interpolation. A conventional background grid was derived for the computational domain. A grid convergence study was conducted with the grid sizes presented in Table 5.

The baseline test conditions for this propeller were based upon the initial starting conditions of the static wind-tunnel test conducted by DOWTY in the 1970s<sup>(5)</sup>. Sea-level conditions were assumed, with the reference velocity and length, for the Reynolds number, selected as the tip Mach number at 1400(rpm) and tip chord length, respectively. Following the convergence of the rigid flow-field at 1400(rpm), the aeroelastic method was then used<sup>(15)</sup>.

A single revolution is used to settle the structural response. Following this, the blade rotational velocity was accelerated from 1400 to 1750(rpm) over 5 revolutions. This acceleration mirrored the process conducted during the experiment. Table 6 details the computational parameters.

A time-step comparison is conducted using  $1^\circ$  and  $0.5^\circ$  steps per propeller revolution.

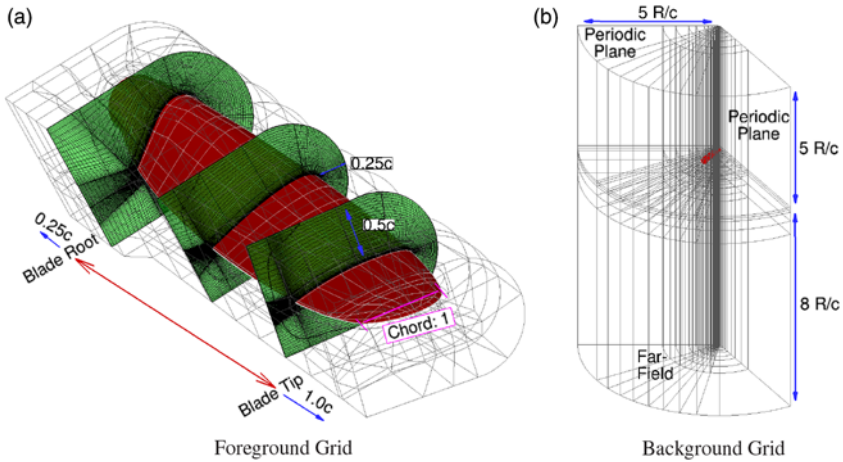


Figure 8. Commander propeller computational domain and chimera grid.

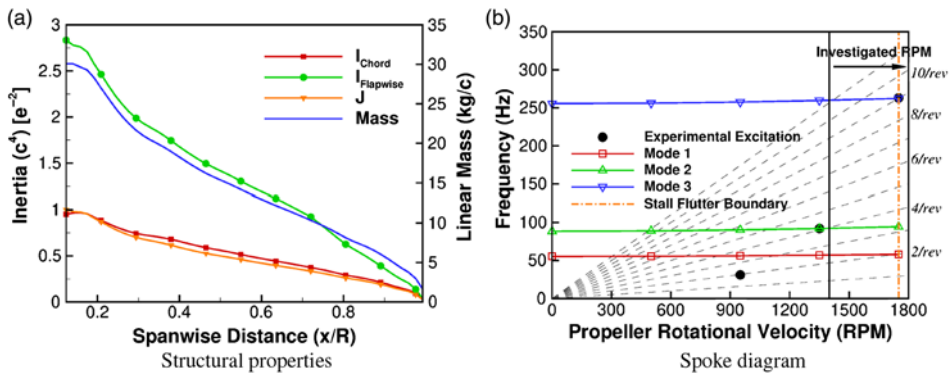


Figure 9. Commander propeller blade structural properties and resultant spoke diagram.

#### 4.2.1 Structural modelling

For the aeroelastic simulation, a NASTRAN structural model is derived to obtain the mode shapes and frequencies for the modal aeroelastic method. The structural model for the Commander blades are based upon the assumption of a solid material blade. The linear mass distribution is calculated as a function of the cross-section area, with the blade inertia based upon the integration of the aerofoil section shape. The blade was assumed to be of 1100 grade aluminum alloy, resulting in a Young's Modulus of 69GPa, Shear Modulus of 26GPa and mass density of 2710kg/m<sup>3</sup>. The cross-sectional area, linear mass and blade sectional inertias are presented in Fig. 9(a). The derived mode shapes match those seen within the experiment, with Fig. 9(b) showing the frequency response compared to the experiment.

In terms of structural damping, a value is supplied to the modal method. For these calculations a transition was made from an initial high value of 0.10 to a final value of 0.001. This allows for the control of the initial aeroelastic response during the first aeroelastic revolution.



**Table 7**  
**Comparison three-dimensional aerodynamic damping estimates for the 3D**  
**URANS and SAS simulations over the entire simulation**

Modelling	Aerodynamic damping		Aerodynamic work
	70%R	90%R	Whole Blade
URANS	0.010	0.035	-2.947
SAS	0.005	-0.004	0.733

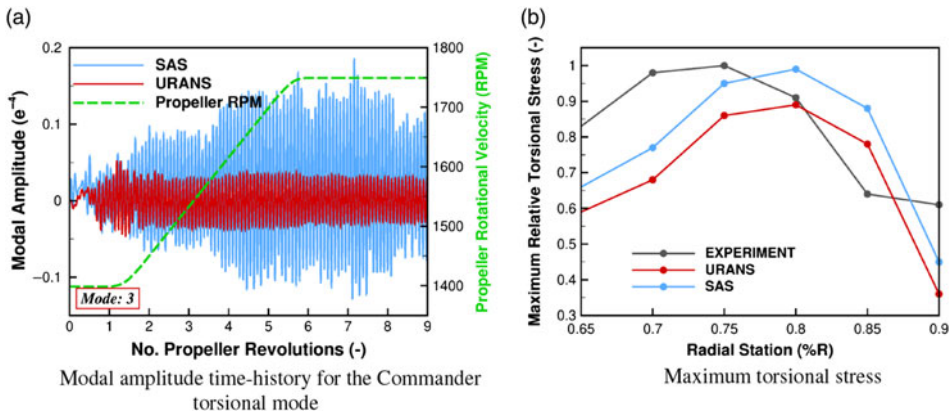


Figure 10. Time history of the modal amplitude results and torsional stress trends across the blade for the aeroelastic validation<sup>(16)</sup>.

### 4.3 Commander propeller blade 3D aerodynamic damping estimation

Presented in Table 7 is the aerodynamic damping estimation from the 3D aeroelastic test case for the *URANS* and *SAS* simulations. As can be seen, and as expected from the dynamic stall study, positive damping values are observed for the *URANS* results, with reduced damping estimations seen for the *SAS*. At the 70% station, the damping estimation reduces by 50%, with the 90% station reducing further producing a negative damping estimation. This reduction in aerodynamic damping for the *SAS* result is also found within the amount of aerodynamic work derived from the entire blade. As observed from Table 7, the *URANS* result produces a negative work estimation with the *SAS* solution producing positive work. From experimental<sup>(5)</sup> and simulation data<sup>(15)</sup>, it is known that this propeller blade is found to suffer from stall flutter. Analysis of the modal amplitudes from the simulation data found the *SAS* results to significantly increase in torsional content with the trend in terms of torsional stress observed across the blade. This is presented in Fig. 10. Through the use of the *SAS* method, the negative aerodynamic damping value associated with stall flutter is achieved.

As previously stated, the 3D aerodynamic damping is estimated using the changes in pitching moment. This is presented in Fig. 11 for the 70% and 90% radial stations. As observed

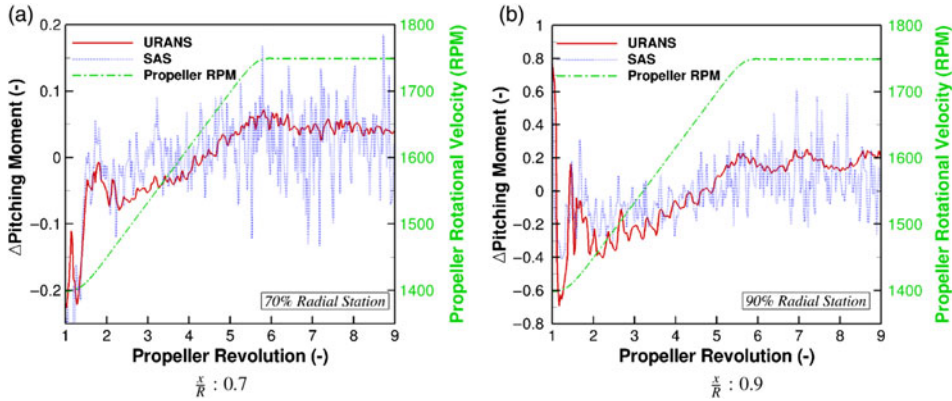


Figure 11. Comparison of the change in pitching moment for the *URANS* and *SAS* simulations.

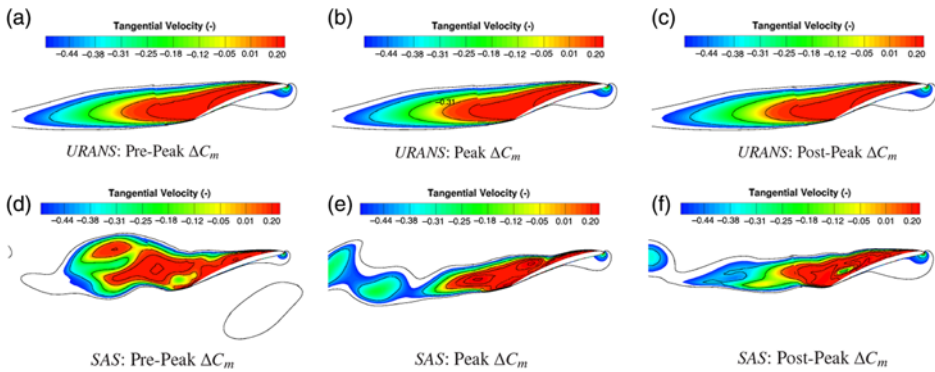


Figure 12. Flow visualisation at  $\frac{x}{R} : 0.9$  of the tangential velocity profile for the *SAS* and *URANS* simulations at maximum  $\Delta C_m$ .

from both *URANS* and *SAS* simulations, there is a significant shift in pitching moment at the start of the first revolution. This is a result of the start-up of the aeroelastic deformations. Following this, oscillations in both *URANS* and *SAS* simulations settle, with a linear increase in the pitching moment found during the transition phase for both radial stations. Examining the profiles for the 70% station, an order of magnitude larger variations in pitching moment are observed during the transition phase for the *SAS* simulation when compared to the *URANS*. This increases to two orders of magnitude following the completion of the acceleration. For the 90% station, a linear trend in pitching moment is also observed during the transition for the *URANS* and *SAS* simulations, however, once the acceleration is complete, significant fluctuations of  $\pm 0.4$  in  $C_m$ , are captured by the *SAS*.

Shown in Fig. 12 is the flow visualisation, using radial slices, of the non-dimensional tangential velocity at the 90% radial station around the maximum change in pitching moment for the *URANS* (a,b,c) and *SAS* (d,e,f) simulations. The tangential velocity is the dominant component across the aerofoil section, therefore, its fluctuations highlight the alterations in detached flow. As can be seen from both the *URANS* and *SAS* results, the 90% station is fully stalled. This results in an entire stall bubble predicted by *URANS*. Very slight changes are

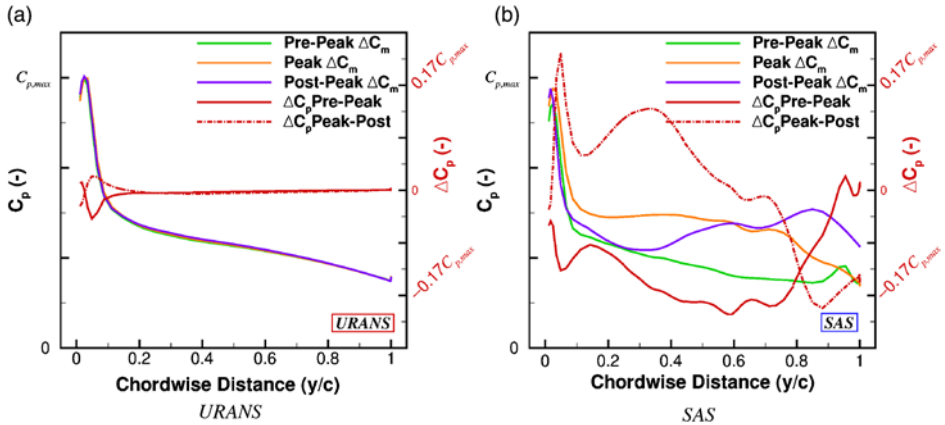


Figure 13. Surface pressure coefficient on the blade upper surface at the 90% radial station through the peak  $\Delta C_m$  for the *URANS* and *SAS* simulations.

observed around the peak value for the *URANS* simulation, in which the detached flow moves towards the leading-edge, thus changing the pressure distribution. The change in pressure distribution on the upper surface, for the *URANS* simulation, is shown in Fig. 13(a). There is a reduction in pressure towards the leading-edge at the peak moment location due to the increase in the stalled flow. This detached flow then travels further downstream causing an increase in pressure which reduces the pitching moment. These changes in surface pressure coefficient, and hence pitching moment, for the *URANS* simulations are small in comparison to the *SAS*.

Looking at the *SAS* flow visualisation results, the structure of the detached flow is significantly different when compared to the *URANS*. For the *URANS*, one singular vortex is produced, whereas the *SAS* method is able to capture the smaller vortex structures which combine to create the entire section wake. Looking at the pre-peak station (Fig. 12(d)), at least five vortical structures can be observed for the *SAS* result. There are three small pockets of detached flow on the blade surface, with two larger structures beginning to shed. As peak pitching moment is reached (Fig. 12(e)), the two larger vortices have shed from the station. This shedding causes a significant reduction in pressure, as observed from Fig. 13(b). Following the shedding of the two larger vortices, the flow attempts to recover post-peak resulting in a positive shift in pressure. It is this process of vortex shedding which causes the larger fluctuations in pitching moment and hence reduced stability in terms of the aerodynamic damping.

To summarise, using the change in pitching moment from its mean and the aeroelastic blade pitch angle, the aerodynamic damping of a given propeller section can be estimated. A comparison of the aerodynamic damping is made of the Commander propeller blade, which is found to be active in torsion, using *URANS* and *SAS* methods. Both observed radial stations, with the *SAS* simulation were found to produce lower levels of aerodynamic damping. This is due to the fact that greater amounts of flow features, such as shedding open stall bubbles, are produced, and therefore cause greater variation in loads and blade deflections. This correlates to the dynamic stall investigations in which the aerodynamic damping is reduced for the quasi-3D *SAS* solutions, and to the model validation<sup>(15)</sup> in which the full 3D aeroelastic simulation using *SAS* was found to flutter, with the *URANS* producing a stable result.

## 5.0 CONCLUSIONS

The following conclusions are drawn from this investigation:

The use of the *SAS* method better approximates the physics associated with stall flutter. Based upon both the aerofoil dynamic stall and full 3D aeroelastic investigations, the *SAS* method is able to capture negative aerodynamic damping estimations. Using the aerodynamic damping estimated from three-dimensional simulations and *SAS*, stall flutter was explored. The three-dimensional results used a time-marching aeroelastic method that captures the characteristics of stall flutter with the use of the *SAS* method.

It has been found that for two-dimensional and three-dimensional test cases, the *SAS* method provides a reduction in the aerodynamic damping, showing clearly the lack of stability for the examined flow conditions. This was in line with the experiment.

Further validation for the method should be performed to increase confidence in the explored numerical techniques. This requires three-dimensional data flow-field data with sectional surface pressure sensors. The combination of experimental flow-field visualisation and pressure coefficients would allow for the tracking of stall interactions and its effect on the blade surface loads. Thus providing an extensive database for propeller stall flutter validation. The study of such flows is fueled by the development of propeller with thinner sections for the expansion of the flight envelope.

## ACKNOWLEDGEMENT

The support provided by DOWTY Propellers is gratefully acknowledged.

## REFERENCES

1. McALISTER, K.W., PUCCI, S.L., McCROSKEY, W.J., and CARR, L.W. An experimental study of dynamic stall on advanced airfoil sections volume 2: Pressure and orce data, *National Aeronautics and Space Administration: Technical Report*, 1982, TM-84245.
2. CARTA, F.O. and NIEBANCK, C.F. Prediction of rotor instability at high forward speeds: Volume III stall flutter, *USAAVLABS: Technical Report*, 1969, 68-18C.
3. McCROSKEY, W.J. The Phenomenon of Dynamic Stall, *National Aeronautics and Space Administration: Technical Memorandum*, 1981, 81264.
4. STERNE, L.H.G. Spinning tests on fluttering propellers, *Aeronautical Research Council: Reports and Memoranda* 1945, 2022.
5. BURTON, P.E. Straingauge test report on a spin test carried out on a type (c) R.305/3-82-F/6 propeller on the spinning tower at the R.A.E. Farnborough, Hants., *DOWTY ROTOL, Technical Report*, 1979, 093.1.592.
6. SMITH, A.F. Analysis and test evaluation of the dynamic stability of three advanced turboprop models at zero forward speeds, *National Aeronautics and Space Administration: Contractor Report*, 1985, 175025.
7. BAKER, J.E. The effects of various parameters, including Mach number, on propeller-blade flutter with emphasis on stall flutter, *National Advisory Commitee for Aeronautics: Technical Report*, 1955, 3357.
8. HUBBARD, H.H., BURGESS, M.F. and SYLVESTER, M.A. Flutter of thin propeller blades, including effects of Mach number, structural damping, and vibratory-stress measurements near the flutter boundaries, *National Advisory Commitee for Aeronautics: Technical Report*, 1956, 3707.
9. REDDY, T.S.R. and KAZA, K.R.V. Analysis of an unswept propfan blade with a semiempirical dynamic stall model, *National Aeronautics and Space Administration: Technical Memorandum*, 1989, 4083.
10. DELAMORE-SUTCLIFFE, D. Modelling of Unsteady Stall Aerodynamics and Prediction of Stall Flutter Boundaries for Wings and Propellers, *PhD Thesis, University of Bristol*, 2007.
11. OGNEV, V. and ROSEN, A. Influence of using various unsteady aerodynamic models on propeller flutter prediction, *Journal of Aircraft*, 2011, **48** (5).

12. DEHAEZE, F. and BARAKOS, G.N. Mesh deformation method for rotor flows, *Journal of Aircraft*, 2012, **49** (1).
13. CHIRICO, G., BARAKOS, G.N. and BOWN, N. Numerical aeroacoustic analysis of propeller designs, *The Aeronautical Journal*, 2018, **122** (1248).
14. BARAKOS, G.N. and JOHNSON, C. Acoustic comparison of propellers, *International Journal of Aeroacoustics*, 2016, **15** (6–7).
15. HIGGINS, R.J., JIMENEZ-GARCIA, A., BARAKOS, G.N. and BOWN, N. A time-marching aeroelastic method applied to propeller flutter, *Proceedings of AIAA SciTech Forum, San Diego, California, USA*, January 2019.
16. HIGGINS, R.J., JIMENEZ-GARCIA, A., BARAKOS, G.N. and BOWN, N. High-fidelity computational fluid dynamics methods for the simulation of propeller stall flutter, *AIAA Journal*, 2019, doi: [10.2514/1.J058463](https://doi.org/10.2514/1.J058463)
17. SCRASE, N. and MAINA, M. The evaluation of propeller aero-acoustic design methods by means of scaled-model testing employing pressure tapped blades and spinner, *19th ICAS Congress*, 1994.
18. GOMARIZ-SANCHA, A., MAINA, M. and PEACE, A.J. Analysis of propeller-airframe interaction effects through a combined numerical simulation and wind-tunnel testing approach, *AIAA SciTech Forum, 53rd AIAA Aerospace Sciences Meeting, Kissimmee, Florida*, 2015.
19. KNEPPER, A. and BOWN, N. IMPACTA Wind-tunnel instrumentation specification, *Dowty Propellers (GE Aviation Systems), Technical Report*, 2014, ITS 01777 (3).
20. BARAKOS, G., STEIJL, R., BADCOCK, K. and BROCKLEHURST, A. Development of CFD capability for full helicopter engineering analysis, *31st European Rotorcraft Forum, Florence, Italy*, 2005.
21. STEIJL, R., BARAKOS, G. and BADCOCK, K. A framework for CFD analysis of helicopter rotors in hover and forward flight, *International Journal of Numerical Methods in Fluids*, 2005, **51**, 8.
22. LAWSON, S., WOODGATE, W., STEIJL, R. and BARAKOS, G. High performance computing for challenging problems in computational fluid dynamics, *Progress in Aerospace Sciences*, 2012, **52**.
23. CROZON, C., STEIJL, R. and BARAKOS, G.N. Coupled flight dynamics and CFD – demonstration for helicopters in shipborne environment *The Aeronautical Journal*, 2018, **122**, 1247.
24. BABU, S.V., LOUPY, G.J.M., DEHAEZE, F., BARAKOS, G.N. and TAYLOR, N.J. Aeroelastic simulations of stores in weapon bays using Detached-Eddy simulation, *Journal of Fluids and Structures*, 2016, **66**.
25. BABU, S.V., ZOGRAFAKIS, G., BARAKOS, G.N. and KUSYUMOV, A. Evaluation of scale-adaptive simulation for transonic cavity flows, *International Journal of Engineering Systems Modelling and Simulation*, 2016, **8** (2).
26. MENTER, F.R. and EGOROV, Y. The scale-adaptive simulation method for unsteady turbulent flow predictions. Part I: Theory and model Description, *Flow, Turbulence and Combustion*, 2010, **85** (1).
27. MENTER, F. R. and EGOROV, Y. A scale adaptive simulation model using two-equation models, *Proceedings of 43rd AIAA Aerospace Sciences Meeting and Exhibit*, 2005.
28. LOUPY, G.J.M., BARAKOS, G.N. and TAYLOR, N.J. Multi-disciplinary simulations of stores in weapon bays using scale adaptive simulation. *Journal of Fluids and Structures*, 2018, **81**.
29. JARKOWSKI, M., WOODGATE, M.A., BARAKOS, G.N. and ROKICKI, J. Towards consistent hybrid overset mesh methods for rotorcraft CFD, *International Journal for Numerical Methods in Fluids*, 2014, **74** (8).
30. CORKE, T.C. and THOMAS, F.O. Dynamic stall in pitching airfoils: Aerodynamic damping and compressibility effects, *Annual Review of Fluid Mechanics*, 2015, **47**.
31. MELLEN, C.P., FRÖHLICH, J. and RODI, W. Lessons from LESFOIL Project on large-eddy-simulation of flow around an airfoil, *AIAA Journal*, 2003, **41** (4).
32. RAMASAMY, M., SANAYEI, A., WILSON, J.S., MARTIN, P.B., HARMS, T., NIKOUEEYAN, P. and NAUGHTON, J. Data-driven optimal basis clustering to characterize cycle-to-cycle variations in dynamic stall measurements, *Proceedings of the Vertical Flight Society 75th Annual Forum and Technology Display*, 2019.